104 *Inorg. Chem.* **2011**, *50*, 104–113
DOI: 10.1021/ic101358q

Inorganic Chemistry
Article

Structures of $Pd(CN)_2$ and $Pt(CN)_2$: Intrinsically Nanocrystalline Materials?

Simon J. Hibble,*,† Ann M. Chippindale,*,† Edward J. Bilbé,† Elena Marelli,† Peter J. F. Harris,‡ and Alex C. Hannon§

†*Department of Chemistry, University of Reading, Whiteknights, Reading RG6 6AD, U.K.,*
‡*Centre for Advanced Microscopy, University of Reading, Reading RG6 6AF, U.K., and*
§*ISIS Facility, Rutherford Appleton Laboratory, Chilton, Didcot OX11 0QX, U.K.*

Received July 8, 2010

Analysis and modeling of X-ray and neutron Bragg and total diffraction data show that the compounds referred to in the literature as "$Pd(CN)_2$" and "$Pt(CN)_2$" are nanocrystalline materials containing small sheets of vertex-sharing square-planar $M(CN)_4$ units, layered in a disordered manner with an intersheet separation of ~3.44 Å at 300 K. The small size of the crystallites means that the sheets' edges form a significant fraction of each material. The $Pd(CN)_2$ nanocrystallites studied using total neutron diffraction are terminated by water and the $Pt(CN)_2$ nanocrystallites by ammonia, in place of half of the terminal cyanide groups, thus maintaining charge neutrality. The neutron samples contain sheets of approximate dimensions 30 Å × 30 Å. For sheets of the size we describe, our structural models predict compositions of $Pd(CN)_2 \cdot xH_2O$ and $Pt(CN)_2 \cdot yNH_3$ ($x \approx y \approx 0.29$). These values are in good agreement with those obtained from total neutron diffraction and thermal analysis, and are also supported by infrared and Raman spectroscopy measurements. It is also possible to prepare related compounds $Pd(CN)_2 \cdot pNH_3$ and $Pt(CN)_2 \cdot qH_2O$, in which the terminating groups are exchanged. Additional samples showing sheet sizes in the range ~10 Å × 10 Å ($y \sim 0.67$) to ~80 Å × 80 Å ($p = q \sim 0.12$), as determined by X-ray diffraction, have been prepared. The related mixed-metal phase, $Pd_{1/2}Pt_{1/2}(CN)_2 \cdot qH_2O$ ($q \sim 0.50$), is also nanocrystalline (sheet size ~15 Å × 15 Å). In all cases, the interiors of the sheets are isostructural with those found in $Ni(CN)_2$. Removal of the final traces of water or ammonia by heating results in decomposition of the compounds to Pd and Pt metal, or in the case of the mixed-metal cyanide, the alloy, $Pd_{1/2}Pt_{1/2}$, making it impossible to prepare the simple cyanides, $Pd(CN)_2$, $Pt(CN)_2$, or $Pd_{1/2}Pt_{1/2}(CN)_2$, by this method.

Introduction

In contrast to many recent studies of nanomaterials, our investigation of the structures of nanocrystalline $Pd(CN)_2$ and $Pt(CN)_2$ was carried out by necessity rather than design. Our initial aim was simply to confirm Pauling's prediction in the "The Nature of the Chemical Bond"[1] that palladium cyanide, and by implication platinum cyanide, has the layer structure shown in Figure 1, based on square-planar $Pd(CN)_4$ units fused together to form a square net. Using total neutron diffraction, we demonstrated recently that similar metal-cyanide layers are found in $Ni(CN)_2$.[2] In addition, the detailed structure of the nickel-cyanide layers was determined and the relationship between neighboring layers established.[2,3] In $Ni(CN)_2$, the near equality of the Ni−C and Ni−N bond lengths means that it is impossible to ascertain using diffraction methods whether there is any ordering of the C≡N groups around the nickel centers. In other cyanide materials, however, where additional evidence is available, for example, from NMR studies of $Cd(CN)_2$[4] and AgCN,[5] disorder of the cyanide groups about the metal centers has been found, in contrast to the ordered C≡N arrangement suggested in Pauling's model.

Our preliminary powder X-ray diffraction (XRD) experiments on $Pd(CN)_2$ and $Pt(CN)_2$ showed that they are much more highly disordered materials than $Ni(CN)_2$, but nevertheless, we believed that using total neutron diffraction we would proceed rapidly to a structural solution. In hindsight, information in the literature should have warned us that the problem might be more complex than we initially envisioned. Both $Pd(CN)_2$ and $Pt(CN)_2$ are described as being difficult to dry with water firmly bound within the structures, and it is stated that the water cannot be completely removed from the platinum-cyanide hydrate, $Pt(CN)_2 \cdot 0.75H_2O$, to form $Pt(CN)_2$ without further decomposition.[6] This behavior contrasts with that of the nickel-cyanide hydrates, $Ni(CN)_2 \cdot nH_2O$ ($1 < n < 3$), which can be easily dehydrated to form anhydrous $Ni(CN)_2$.[2]

*To whom correspondence should be addressed. E-mail: s.j.hibble@rdg.ac.uk (S.J.H.), a.m.chippindale@rdg.ac.uk (A.M.C.).

(1) Pauling, L. In *The Nature of the Chemical Bond*, 3rd ed.; Cornell University Press: Ithaca, NY, 1960; Chapter 6, p 169.
(2) Hibble, S. J.; Chippindale, A. M.; Pohl, A. H.; Hannon, A. C. *Angew. Chem., Int. Ed.* **2007**, *46*, 7116.
(3) Goodwin, A. L.; Dove, M. T.; Chippindale, A. M.; Hibble, S. J.; Pohl, A. H.; Hannon, A. C. *Phys. Rev.* **2009**, *B80*, 54101.
(4) Nishikiori, S.; Ratcliffe, C. I.; Ripmeester, J. A. *Can. J. Chem.* **1990**, *68*, 2270.
(5) Bryce, D. L.; Wasylishen, R. E. *Inorg. Chem.* **2002**, *41*, 4131.
(6) (a) Baranovskii, I. B.; Kharitonov, Y. Y. *Doklady Akad. Nauk. SSSR* **1966**, *169*, 805. (b) Sharpe, A. G. In *The Chemistry of Cyano Complexes of the Transition Metals*; Academic Press: London, 1976; Chapter 9, p 248.

 Published on Web 11/30/2010

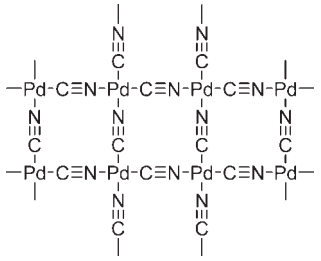

Figure 1. Pauling's proposed structure of a sheet of $Pd(CN)_2$.[1]

In this work, we prove that the basic structures of $Pd(CN)_2$ and $Pt(CN)_2$ are indeed layered and assembled from vertex-sharing square-planar $M(CN)_4$ units and determine the detailed structures from total neutron diffraction. The X-ray and neutron diffraction studies, carried out on dried commercially supplied palladium cyanide (**I**) and platinum cyanide (**II**), synthesized in-house by decomposition of $(NH_4)_2[Pt(CN)_4]\cdot 2H_2O$, also establishes that these materials are nanocrystalline with sheet size ~30 Å × 30 Å. Palladium and platinum are four coordinate, and charge neutrality in these nanocrystals is maintained by replacing half of the terminal C≡N groups at the corners and edges of the sheets by H_2O or NH_3 groups respectively to yield compositions $Pd(CN)_2\cdot xH_2O$ ($x = 0.29$) (**I**) and $Pt(CN)_2\cdot yNH_3$ ($y = 0.29$) (**II**). Other routes to nanocrystalline palladium and platinum cyanides with a range of crystallite sizes (**IV-IX**) are also reported. For palladium cyanide, these include the thermal decomposition of *cis*-$Pd(CN)_2(NH_3)_2$ and its reaction with ethanoic acid, and for platinum cyanide, the reaction of $K_2Pt(CN)_4$ with K_2PtCl_4 in aqueous solution. These methods yield $Pd(CN)_2\cdot pNH_3$ (**V**, **VI**) and $Pt(CN)_2\cdot qH_2O$ (**VIII**), demonstrating that it is possible to prepare ammonia- and water-terminated materials for both palladium and platinum cyanide. The smallest sheets prepared were ~10 Å × 10 Å for $Pt(CN)_2\cdot qH_2O$ ($q = 0.67$) (**VIII**). The high q value is a result of the small sheet size. Larger sized sheets of ~80 Å × 80 Å, were produced for $Pd(CN)_2\cdot xH_2O$ ($x = 0.12$) (**IV**) by annealing under hydrothermal conditions, and it was also possible to prepare a mixed-metal cyanide, $Pd_{1/2}Pt_{1/2}(CN)_2\cdot xH_2O$ ($x = 0.50$) (**IX**).

Results and Discussion

X-ray Diffraction. Figure 2 shows the powder XRD patterns for $Pd(CN)_2\cdot 0.29H_2O$ (**I**) and $Pt(CN)_2\cdot 0.29NH_3$ (**II**). The palladium and platinum cyanides are clearly much less crystalline than $Ni(CN)_2$.[2] Their powder patterns are not suitable for structure determination as they only contain a small number of very broad Bragg reflections, indicating very small crystallite sizes. However, the close resemblance of the two patterns to each other suggests that the palladium and platinum materials are isostructural. Considering the proposed structure of the layer (Figure 1) and, by analogy with the known tetragonal structure of $Ni(CN)_2$, the first peak (2θ ~18.3°, d ~ 4.84 Å) might be assigned as the (*100*) reflection. For compounds (**I**) and (**II**) however, only two indices, (*hk*), are required to index completely the diffraction patterns. Unlike in the case of $Ni(CN)_2$, there are no sharp intense peaks corresponding to (*00l*) reflections indicating that the crystallite dimensions in the *c* direction must be very small. There is thus no information obtainable from Bragg diffraction on the third dimension.

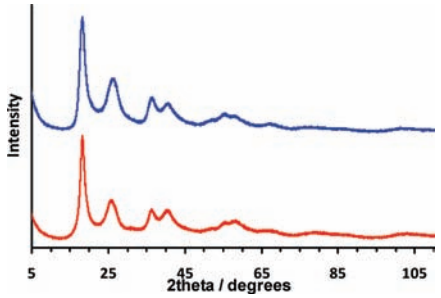

Figure 2. Powder XRD data for $Pd(CN)_2\cdot 0.29H_2O$ (**I**) (blue) and $Pt(CN)_2\cdot 0.29NH_3$ (**II**) (red) measured at room temperature.

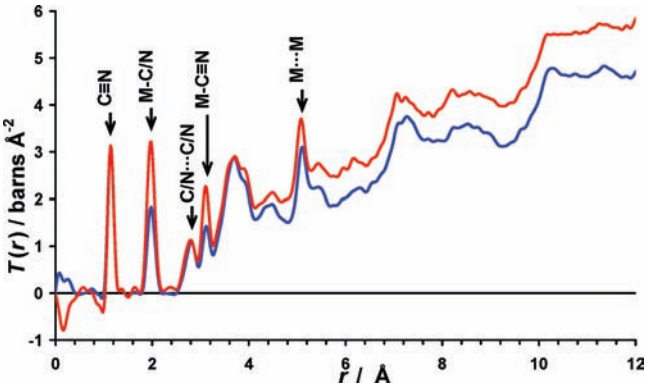

Figure 3. Total correlation functions, $T(r)_{exp}$, for $Pd(CN)_2\cdot 0.29H_2O$ (**I**) (blue) and $Pt(CN)_2\cdot 0.29NH_3$ (**II**) (red) at 10 K. The peaks at low r (< 4 Å) correspond to single correlations. (*N.B.* The peaks corresponding to the C≡N correlations in both compounds completely overlap). The intense peak at ~5 Å yields the M···M distance but also contains contributions from other atom pairs.

The Scherrer equation[7] applied to the first reflection, (*10*), yields sheet dimensions of ~50 × 50 Å for both $Pd(CN)_2\cdot 0.29H_2O$ (**I**) and $Pt(CN)_2\cdot 0.29NH_3$ (**II**). The results of the total neutron diffraction experiments are required for a more detailed analysis of the layer structure and to obtain more accurate sheet sizes by modeling the X-ray data (*vide infra*).

Neutron Diffraction. From the neutron diffraction experiments at 10 K, the total pair correlation functions, $T(r)_{exp}$ (Figure 3) for $Pd(CN)_2\cdot 0.29H_2O$ (**I**) and $Pt(CN)_2\cdot 0.29NH_3$ (**II**), were obtained by Fourier transformation of $Qi(Q)$ to generate $D(r)_{exp}$, followed by addition of the average scattering density.[8] Maxima in $T(r)_{exp}$ correspond to frequently occurring interatomic distances in the compounds, and, at low r, can often be ascribed to "chemical bonds".[9] Thus in the $Pd(CN)_2\cdot 0.29H_2O$ (**I**) and $Pt(CN)_2\cdot 0.29NH_3$ (**II**) correlation functions, the peaks at ~1.15 and ~1.98 Å correspond to the C≡N and M−C/N bond distances respectively. The equality, or near equality, of the M−C and M−N bond lengths is not unexpected, as it has been observed in a number of other metal cyanides, for example, in $Ni(CN)_2$[3] and the group 11

(7) Klug, H. P.; Alexander, L. E. In *X-Ray Diffraction Procedures for Polycrystalline and Amorphous Materials*, 2nd ed.; John Wiley & Sons Inc.: New York, 1974; Chapter 9, p 687. The mean crystallite dimension, τ, in the direction corresponding to the reflection is given by $\tau = (K\lambda)/\beta \cos\theta$, where K is the shape factor (taken as 0.9), λ is the X-ray wavelength (1.54060 Å), β is the line broadening at half the maximum intensity (FWHM) in radians, and θ is the Bragg angle.

(8) Keen, D. A. *J. Appl. Crystallogr.* **2001**, *34*, 172.

(9) (a) Billinge, S. J. L.; Kanatzidis, M. G. *Chem. Commun.* **2004**, 749. (b) Hibble, S. J.; Hannon, A. C.; Fawcett, I. D. *J. Phys. Cond. Matter* **1999**, *11*, 9203.

Table 1. Interatomic Distances Obtained from $T(r)_{exp}$ for $Pd(CN)_2 \cdot 0.29H_2O$ (**I**) and $Pt(CN)_2 \cdot 0.29NH_3$ (**II**)

	$Pd(CN)_2$ **(I)**	$Pd(CN)_2$ **(I)**	$Pt(CN)_2$ **(II)**	$Pt(CN)_2$ **(II)**
	10 K	300 K	10 K	300 K
$r_{C\equiv N}$ /Å	1.1487(8)	1.1580(8)	1.152(1)	1.1576(8)
$r_{M\text{-}C/N}$ /Å	1.985(2)	1.983(2)	1.978(2)	1.979(1)
$r_{C/N\ldots C/N}$ /Å	2.806(1)	2.807(2)	2.788(3)	2.792(1)
$r_{M\text{-}C\equiv N}$ /Å, $r_{M\text{-}N\equiv C}$ /Å	3.1156(6)	3.113(1)	3.1074(8)	3.1085(6)
$r_{M\ldots M}$ /Å	5.0988(2)	5.0869(4)	5.0787(2)	5.0709(1)
$a_{T(r)}{}^{\dagger}$ /Å	5.119	5.124	5.108	5.116

$^{\dagger} a_{T(r)} = (2r_{M-Z} + r_{C\equiv N})$.

cyanides, CuCN,[10] AgCN,[11] and AuCN.[12] It must be emphasized that this information on bond lengths is directly obtained and independent of any structural model. The third peak, at ~2.80 Å in both cases, confirms that the coordination geometry around palladium and platinum is square planar and the fourth, at ~3.11 Å, that the sheets are flat (Table 1) as predicted by Pauling,[1] as found also in $Ni(CN)_2$.[2,3] The sharp peaks at ~5.09 Å correspond to the intralayer repeats, for example, Pd-(CN)-Pd in Figure 1. The first Bragg peaks in the XRD patterns for both materials occur at d = ~4.8 Å rather than at 5.1 Å, as would be the case if they were extended solids. This is consistent with their nanocrystallinity as discussed in the X-ray Modeling Section below.

Over the full $T(r)$ range shown (Figure 3), the peaks in both correlation functions occur at almost identical positions providing further confirmation that the two materials are isostructural. The differences in peak intensities in the two correlation functions arise because of the smaller scattering length of palladium compared to platinum. The intensities of peaks not involving metal atoms, for example, the peak at ~1.15 Å due to the C≡N correlations in the two materials, are identical in the two $T(r)_{exp}$ plots. The divergence of the plots on increasing r reflects the different average scattering density of the two materials. The troughs in $T(r)_{exp}$ at ~1 Å, just to the left of the peaks due to C≡N, and most evident in the platinum-cyanide correlation function, arise from the O−H and N−H correlations in palladium and platinum cyanides, respectively.

Modeling $T(r)_{exp}$. (i). Bulk Structure of the Nanoparticles. Having established the chemically expected regular square-planar coordination around the M^{2+} ions, it is necessary to model the structure at longer length scales to confirm unequivocally that Pauling's sheet model is correct and also to determine how neighboring sheets stack together. At higher r, many correlations overlap in $T(r)_{exp}$ making it impossible to extract individual distances directly. However, $T(r)$ can be calculated for any structural model and compared with that obtained experimentally. It should be emphasized at this point that total neutron diffraction is rather insensitive to C≡N order/disorder in the palladium and platinum cyanides as a consequence of the equality of the M−C and M−N bond lengths, and it is appropriate to use a *pseudo* atom, Z, with a scattering length, b_Z, equal to $(0.5b_C + 0.5b_N)$ in place of distinct carbon or nitrogen atoms. The models we use are crystallographic and require a set of lattice parameters, a space group, and atomic coordinates. An individual sheet has effective *p4mm* symmetry (plane group no. 11) if we assume that C and N are indistinguishable and assume a single M−Z bond distance. The sum of the bond lengths $(2r_{M-Z} + r_{C\equiv N})$ obtained from the peaks at low r in $T(r)_{exp}$ (Table 1) gives an effective lattice parameter, $a_{T(r)}$, from which the fractional atomic coordinates, x and y, can be derived. It should be noted that the value of $a_{T(r)}$ is always larger than the corresponding $r_{M\ldots M}$ value (Table 1) because even at low temperatures, M−CN−M bending motions draw the metal atoms closer together.

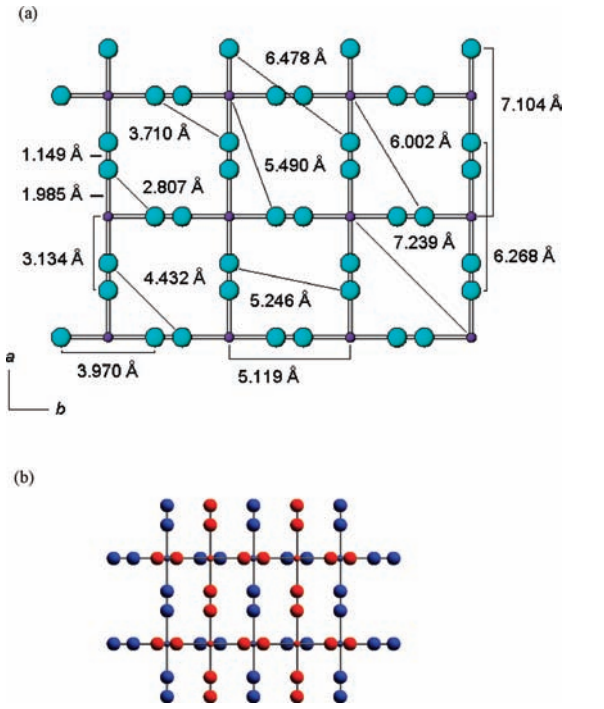

Figure 4. (a) Portion of a $Pd(CN)_2$ layer showing interatomic distances calculated assuming *p4mm* symmetry and using the C≡N and Pd−C/N bond lengths taken from $T(r)_{exp}$ at 10 K (Key: Pd, purple spheres; C/N, cyan spheres), (b) a projection showing how nearest-neighbor layers (shown in red and blue) stack.

The interlayer separation was estimated from density measurements to be ~3.4 Å. This value agrees with that obtained by scaling the interlayer separation found for $Ni(CN)_2$ using the ratio of $r_{Pt\text{-}Z}/r_{Ni\text{-}Z}$. Subsequent modeling of the correlation functions, $T(r)_{exp}$, yielded final values for the interlayer separations at 10 and 300 K of 3.40 and 3.44 Å for both Pd and Pt materials.

Plausible ways of stacking sheets together whilst retaining *p4mm* sheet symmetry were then explored. Models with metal atoms stacked above each other, as in $K_2Pt(CN)_4Br_{0.3} \cdot 3H_2O$,[13] did not reproduce $T(r)_{exp}$ well and were rejected. Only models incorporating offset nearest neighbor stacking arrangements of the type shown in Figure 4 produced satisfactory agreement with $T(r)_{exp}$ in each case. These models, in spacegroups $I4_1/amd$ and $P4_2/mmc$,

(10) Hibble, S. J.; Cheyne, S. M.; Hannon, A. C.; Eversfield, S. G. *Inorg. Chem.* **2002**, *41*, 4990.
(11) (a) Hibble, S. J.; Cheyne, S. M.; Hannon, A. C.; Eversfield, S. G. *Inorg. Chem.* **2002**, *41*, 1042. (b) Reckeweg, O.; Lind, C.; Simon, A.; DiSalvo, F. J. *Z. Naturforsch.* **2003**, *B58*, 155.
(12) Hibble, S. J.; Hannon, A. C.; Cheyne, S. M. *Inorg. Chem.* **2003**, *42*, 4724.
(13) Heger, G.; Deiseroth, H. J.; Schulz, H. *Acta Crystallogr.* **1978**, *B34*, 725.

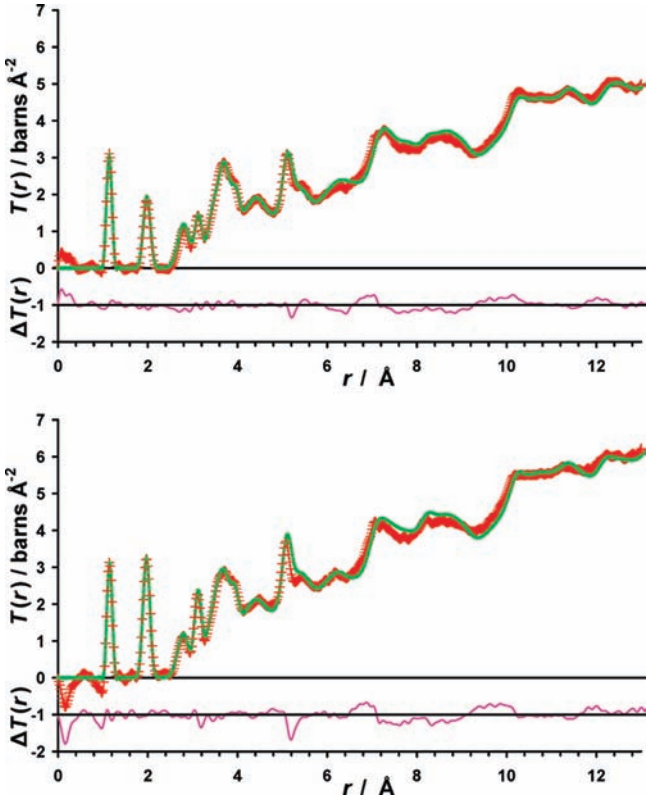

Figure 5. Experimental total pair correlation functions $T(r)_{exp}$ (red crosses) and $T(r)_{model}$ (green line) for $Pd(CN)_2$ (**I**) (top) and $Pt(CN)_2$ (**II**) (bottom) at 10 K. The difference plot, shown in pink, is shifted on the vertical axis by −1.

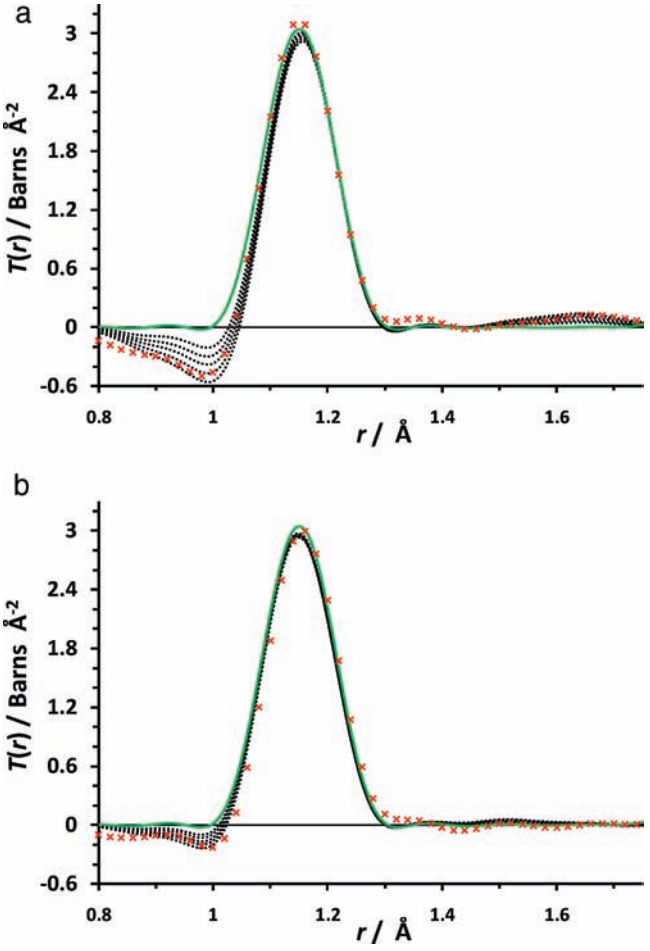

Figure 6. (a) Modeling the low r region of $T(r)$ for $Pt(CN)_2 \cdot yNH_3$. $T(r)_{exp}$ (red crosses), $T(r)_{model}$ for $y = 0$ (green line), and $T(r)_{model}$ for $y = 0.1$, 0.15, 0.20, 0.25, and 0.30 (black dotted curves, with $y = 0.30$ reaching the most negative value). (b) Modeling the low r region of $T(r)$ for $Pd(CN)_2 \cdot xH_2O$. $T(r)_{exp}$ (red crosses), $T(r)_{model}$ for $x = 0$ (green line), and $T(r)_{model}$ for $x = 0.1$, 0.15, 0.20, 0.25, and 0.30 (black dotted curves, with $x = 0.30$ reaching the most negative value).

generate the same nearest-neighbor but different next-nearest neighbor sheet offsets. There was no significant difference in the agreement between $T(r)_{exp}$ and $T(r)_{calc}$ for models in these two spacegroups even beyond $r \sim 6.8$ Å where small differences would begin to be apparent if these were well-ordered crystalline materials because of the different sheet packing. However, there is a very high degree of interlayer disorder in the actual materials which is reflected in the much higher root-mean-square displacements needed to broaden the interlayer correlations than are needed to broaden the intralayer (in sheet) correlations (see Supporting Information). This difference is even more pronounced than in the case of $Ni(CN)_2$[2] and is consistent with the fact that no information about the third dimension is seen in the Bragg diffraction patterns from palladium and platinum cyanides in contrast to nickel cyanide.

The model in $I4_1/amd$ was chosen because this requires fewer sets of fractional coordinates to define the structure; namely, one for M and one for Z. Further details of the modeling are given in the Supporting Information. Figure 5 shows $T(r)_{model}$ plots calculated in spacegroup $I4_1/amd$ which reproduce $T(r)_{exp}$ well.

(ii). Edges of the Nanoparticles. One feature visible in both $T(r)_{exp}$ plots for compounds (**I**) and (**II**), and not yet accounted for, is a trough at ~1 Å. This feature must arise from correlations involving hydrogen. Such correlations produce troughs rather than peaks in the plots of $T(r)_{exp}$ because hydrogen has a negative coherent scattering length. This feature is more pronounced in the platinum-cyanide case. On the basis of the relative intensities of these features, these can be ascribed to N−H correlations from NH_3 groups in the platinum-cyanide case and to O−H correlations from H_2O in the palladium-cyanide case. The ratio of the intensities of the troughs for equimolar amounts of NH_3 and H_2O calculated from the coherent scattering lengths of the appropriate atoms, b_c, and the number of N−H and O−H correlations $((6b_Nb_H)/4b_Ob_H))$ is 2.42. Figure 6a shows a portion of the low r region of $T(r)_{exp}$, together with calculations of models of $Pt(CN)_2 \cdot yNH_3$ with $(0.0 \le y \le 0.3)$. The best agreement is for $y \approx 0.30$. The presence of NH_3 groups also predicts that a small positive peak arising from H···H correlations in the molecule should occur at 1.62 Å, which is indeed observed. The amounts of water and ammonia in the two compounds are equal, and in the case of $Pd(CN)_2 \cdot xH_2O$ (Figure 6b), $x \approx 0.30$ also gives a good fit to $T(r)_{exp}$. These x and y values are in good agreement with the thermogravimetric analysis for these materials (Table 3). In line with the modeling of the X-ray data described below, we assign the compositions of these materials as $Pd(CN)_2 \cdot 0.29H_2O$ (**I**) and $Pt(CN)_2 \cdot 0.29NH_3$ (**II**).

The presence of significant amounts of water and ammonia in these palladium and platinum cyanides is a consequence of their nanocrystalline nature. In nanocrystalline materials, terminating groups represent a significant fraction of the material composition. Water and ammonia play this

Table 2. Relationship Between Model Sheet Size and the Composition in Nanocrystalline $Pd(CN)_2$ and $Pt(CN)_2$, Together with the Calculated Ratio of Terminal:Bridging Cyanide Groups

	sheet size[a] (Å × Å)					
	1 × 1 (5 × 5)	2 × 2 (10 × 10)	3 × 3 (15 × 15)	4 × 4 (20 × 20)	5 × 5 (25 × 25)	6 × 6 (30 × 30)
n for $M(CN)_2 \cdot nH_2O$ and $M(CN)_2 \cdot nNH_3$	1.00	0.67	0.50	0.40	0.33	0.29
(no. terminal CN)/(no. bridging CN)	1	1/2	1/3	1/4	1/5	1/6
	sheet size[a] (Å × Å)					
	7 × 7 (35 × 35)	8 × 8 (40 × 40)	9 × 9 (45 × 45)	10 × 10 (50 × 50)	11 × 11 (55 × 55)	20 × 20 (100 × 100)
n for $M(CN)_2 \cdot nH_2O$ and $M(CN)_2 \cdot nNH_3$	0.25	0.22	0.20	0.18	0.17	0.10
(no. terminal CN)/(no. bridging CN)	1/7	1/8	1/9	1/10	1/11	1/20

[a] Sheet size is expressed in terms of number of M−CN−M repeats and the corresponding length (assuming that the M−CN−M repeat is ~5 Å).

Table 3. Sheet Sizes and Compositions for the Neutron Samples $Pd(CN)_2 \cdot xH_2O$ (**I**) and $Pt(CN)_2 \cdot yNH_3$(**II**) Determined and Derived by a Variety of Methods[a]

	$Pd(CN)_2 \cdot xH_2O$ (**I**)		$Pt(CN)_2 \cdot yNH_3$(**II**)	
experimental method	x	sheet size/Å × Å	y	sheet size/Å × Å
from width of (*10*) reflection in powder XRD[b]	*0.18*	**50 × 50**	*0.15*	**60 × 60**
from modeling powder XRD[c]	*0.29*	**30 × 30**	*0.29*	**30 × 30**
$TGA_{>100\ °C}$[d]	**0.29**	*30 × 30*	**0.22**	*40 × 40*
modeling peak at ~1 Å in $T(r)_{exp}$	**0.30**	*30 × 30*	**0.30**	*30 × 30*
from longest-range correlations in $D(r)$[e]	*~0.29*	**~30 × 30**	*~0.29*	**~30 × 30**

[a] Experimentally determined values are given in **bold** and derived ones in *italics* from information in Table 2. [b] Sheet size determined using the Scherrer equation.[7] [c] Sheet size determined by comparison of the experimental powder XRD pattern with those calculated for a range of sheet sizes (Figure 9). [d] Composition determined from TGA using weight loss at T > 100 °C (see Supporting Information). [e] Assuming square sheets, each sheet edge is (longest correlation)/$\sqrt{2}$ (Figure 8).

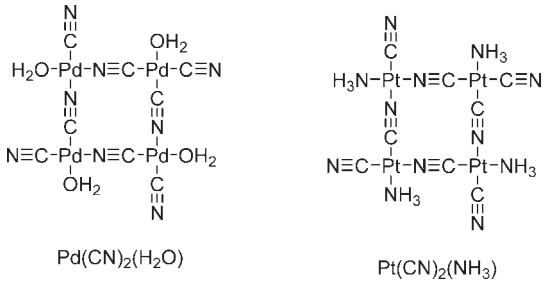

Figure 7. The ultimate nanoparticles, $Pd_4(CN)_8(H_2O)_4$ and $Pt_4(CN)_8(NH_3)_4$ with their corresponding empirical formulae.

role in these materials. Figure 7 shows the ultimate nanoparticles, $Pd_4(CN)_8(H_2O)_4$ and $Pt_4(CN)_8(NH_3)_4$, in which four water or ammonia molecules are required to maintain the square-planar coordination around the metal atoms whilst achieving charge neutrality. The empirical formulae of these nanoparticles, $Pd(CN)_2 \cdot xH_2O$ and $Pt(CN)_2 \cdot yNH_3$, have $x = y = 1$. The sheet sizes of the nanoparticles with $x = y = 0.29$ clearly must be larger than these. Table 2 shows how x and y depend on the sheet size (in terms of both Pt−CN−Pt or Pd−CN−Pd repeats and Å), assuming that both charge neutrality and square-planar coordination around M are maintained. The further assumption of square sheets not only simplifies the table, but proves to be reasonable in the X-ray modeling study. Using Table 2, sheet sizes of 30 Å × 30 Å (6 × 6 M−CN−M repeats) are obtained for both $Pd(CN)_2 \cdot 0.29H_2O$ (**I**) and $Pt(CN)_2 \cdot 0.29NH_3$ (**II**), which are a little smaller than the crystallite sizes obtained from the Scherrer equation (Table 3). The sheet sizes obtained for $Pd(CN)_2 \cdot 0.29H_2O$ (**I**) and $Pt(CN)_2 \cdot 0.29NH_3$ (**II**) determined and derived using a variety of methods are given in Table 3.

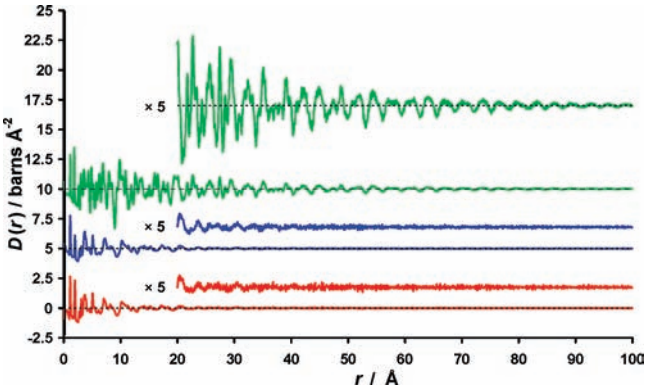

Figure 8. Differential correlation function, $D(r)_{exp}$, for $Pt(CN)_2 \cdot 0.29NH_3$ (**II**) (red), $Pd(CN)_2 \cdot 0.29H_2O$ (**I**) (blue) (offset by 5 barns $Å^{-2}$) and $Ni(CN)_2$ (green),[2] (offset by 10 barns $Å^{-2}$). $D(r)_{exp}$ is also shown for each compound with 5-fold magnification over the region 20−100 Å.

The correlation function, $D(r)_{exp}$, further confirms the small-sheet sizes of both palladium and platinum cyanides (Figure 8). No correlations are visible in $D(r)_{exp}$ beyond ~42 Å. Assuming this value corresponds to a maximum M···M distance across the sheet diagonal for a square sheet, this gives a sheet edge of $42/\sqrt{2} \approx 30$ Å, that is, a sheet size of 30 Å × 30 Å. $D(r)_{exp}$ for $Ni(CN)_2$, also determined using data from the GEM diffractometer[2] (Figure 8), has correlations clearly visible even at 100 Å. This highlights the differences between nanocrystalline palladium and platinum cyanides, consisting of short stacks of small sheets and disordered crystalline nickel cyanide, with essentially the same structure, in which there are a greater number of more extensive (effectively infinite) sheets per stack.

Modeling of X-ray Bragg Diffraction Data. X-ray Bragg diffraction patterns were calculated using the

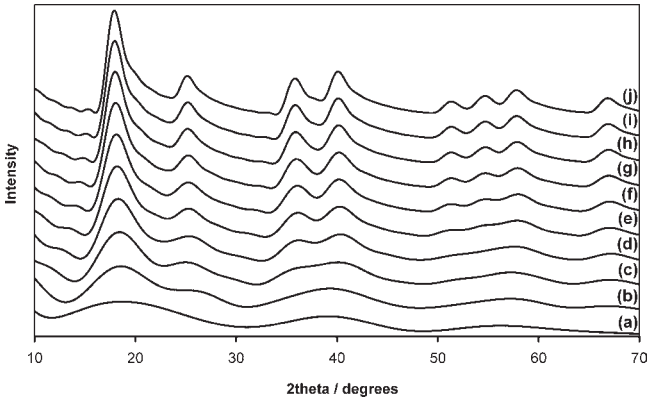

Figure 9. Calculated XRD patterns for $Pt(CN)_2$ sheets with sheet sizes varying from (a) 5 Å × 5 Å (1 × 1 Pt−CN−Pt repeat unit) to (j) 50 Å × 50 Å (10 × 10 Pt−CN−Pt repeat units) in increments of 5 Å × 5 Å.

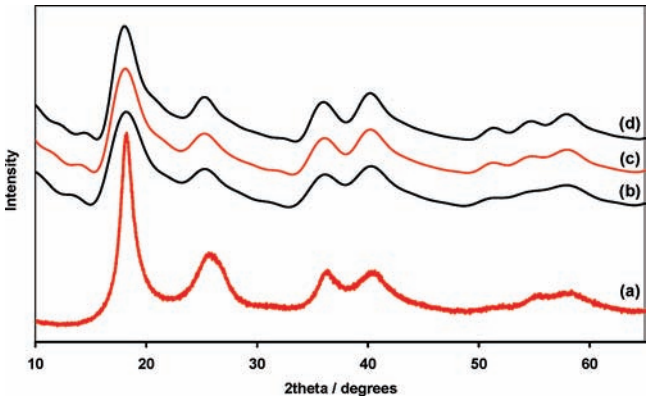

Figure 10. Experimental XRD pattern of (a) $Pt(CN)_2 \cdot 0.29NH_3$ (**II**) compared to calculated patterns for $Pt(CN)_2$ sheets with sheets sizes of (b) 25 Å × 25 Å, (c) 30 Å × 30 Å, and (d) 35 Å × 35 Å.

DISCUS program[14] for individual $Pd(CN)_2$ and $Pt(CN)_2$ square sheets with *p*4*mm* symmetry, but with differing extents. In each case, the M···M distance (i.e., M−CN−M repeat) from $T(r)_{exp}$ was used as the lattice parameter with the metal atom M placed at the origin and atom *Z* at (x, 0) so as to reproduce the M−Z distance determined from the correlation function (Table 1). The modeling of the X-ray data of platinum cyanide shows that the peak positions, shapes, and widths all vary as a function of the sheet extent (Figure 9). The shifts in peak positions, at first sight a deviation from Bragg's Law, is a consequence of the small extent of the sheets. Such behavior has been observed previously, for example, in the classic paper by Warren[15] and more recently in turbostratic carbon.[16] These papers also show how peak shapes vary with the dimensions of the crystallites. A comparison of the experimental pattern for $Pt(CN)_2 \cdot 0.29NH_3$ (**II**) with the calculated patterns shows that the sheets sizes must lie in the range 25 Å × 25 Å to 35 Å × 35 Å (Figure 10). The calculated diffraction pattern shown in Figure 10c with a 30 Å × 30 Å (6 × 6 Pt−CN−Pt repeats) sheet size, not only has the overall appearance of the experimental pattern, but correctly predicts the position of the first peak at ∼18.3° 2θ. This sheet size is in good agreement with the sizes obtained using other methods (Table 3). In an infinite solid, the first peak, corresponding to the (*10*) reflection, would occur at 5.0709 Å, the Pt···Pt distance (Table 1), whereas in $Pt(CN)_2 \cdot 0.29NH_3$(**II**), the *d*-spacing is 4.84 Å because of the small crystallite size. The simulations for palladium cyanide (Supporting Information, Figure S.4) show similar behavior, also yielding a sheet size of 30 Å × 30 Å for $Pd(CN)_2 \cdot 0.29H_2O$ (**I**). Remarkably, these two-dimensional models can account for the experimental XRD patterns and no (*00l*) or (*hkl*) reflections are observed. This behavior is consistent with the high degree of disorder as seen in the interlayer correlations determined from the total neutron diffraction study. In contrast, in the X-ray pattern of $Ni(CN)_2$, the interlayer reflections are very sharp indicating that hundreds, if not thousands, of sheets are stacked together.[2,3]

Further Syntheses of Nanocrystalline Materials. Additional nanocrystalline palladium and platinum cyanides were prepared (**IV**)−(**IX**) including examples in which the terminating groups were varied; that is, palladium-cyanide nanoparticles terminated by ammonia, $Pd(CN)_2 \cdot pNH_3$, and platinum-cyanide nanoparticles terminated by water, $Pt(CN)_2 \cdot qH_2O$ (Table 4). Rational syntheses of $Pd(CN)_2 \cdot pNH_3$ and $Pt(CN)_2 \cdot yNH_3$ were achieved by heating the crystalline precursors, *cis*-$Pd(CN)_2(NH_3)_2$ and *cis*-$Pt(CN)_2(NH_3)_2$, which have ammonia and cyanide already attached to the metal centers. The synthetic method used to prepare $Pt(CN)_2 \cdot qH_2O$, involving the reaction of $Pt(CN)_4^{2-}$ and $PtCl_4^{2-}$, was easily modified to produce a mixed palladium−platinum cyanide, $Pd_{1/2}Pt_{1/2}(CN)_2 \cdot 0.50H_2O$ by replacing $Pt(CN)_4^{2-}$ by $Pd(CN)_4^{2-}$. The sheet sizes for compounds (**V**)−(**IX**), as determined by X-ray modeling and the Scherrer equation, were smaller than those found for the neutron samples (**I**) and (**II**) and are in reasonable agreement with the *p* and *q* values determined from thermogravimetric analysis (TGA) (Table 4). The smallest sheet size produced was 10 Å × 10 Å in $Pt(CN)_2 \cdot 0.67H_2O$ (**VIII**), which clearly shows much broader reflections in the XRD pattern compared to $Pt(CN)_2 \cdot 0.29NH_3$ (**II**) (Figure 11). The sheet, complete with terminating water molecules, is shown in Figure 12. Attempts to produce highly crystalline $Pd(CN)_2$ and $Pt(CN)_2$ by heating nanocrystalline samples in an autoclave in water with a small amount of KCN, to act as a mineralizer, were not successful. This hydrothermal treatment of palladium cyanide produced $Pd(CN)_2 \cdot 0.12H_2O$ (**IV**), which shows only a moderate increase in sheet size, determined from X-ray modeling as 80 Å × 80 Å, and the onset of interlayer ordering (Supporting Information, Figure S5). In the behavior of the shift in the position of the (*10*) peak as a function of peak width (Figure 13), the compounds (**I**)−(**IX**) all lie on a common curve reinforcing the idea that they form a family.

Vibrational Spectra. The vibrational spectra of the palladium and platinum cyanide materials provide supporting information on the sheet sizes and their terminating groups (Figures 14, 15 and 16). Coordinated ammonia and water both show vibrations at ∼1600 cm^{-1} in the IR corresponding to $\delta_{as}(NH_3)$ and $\delta(OH_2)$ respectively, but they can be distinguished because the ammonia-containing compounds show an additional vibration, $\delta_s(NH_3)$, in the region 1200−1300 cm^{-1}. Our models for nanocrystalline palladium and platinum cyanides, which are of finite extent, predict the presence of two types of cyanide group, namely, bridging and terminal, as illustrated in Figure 12: only bridging

(14) Proffen, T.; Neder, R. B. *J. Appl. Crystallogr.* **1997**, *30*, 171.
(15) Warren, B. E. *Phys. Rev.* **1941**, *59*, 693.
(16) Fujimoto, H. *Carbon* **2003**, *41*, 1585.

Table 4. Summary of Nanocrystalline Palladium and Platinum Cyanides, $M(CN)_2 \cdot nH_2O$ and $M(CN)_2 \cdot nNH_3$, Together with Their Corresponding Sheet Sizes and Compositions

	sample (origin)	terminal groups	sheet size/Å × Å	$n_{derived}$	n_{TGA}[c]
I	$Pd(CN)_2 \cdot nH_2O$ (neutron sample)	H_2O	30 × 30[a] 50 × 50[b]	0.29[a] 0.18[b]	0.29
II	$Pt(CN)_2 \cdot nNH_3$ (neutron sample)	NH_3	30 × 30[a] 60 × 60[b]	0.29[a] 0.15[b]	0.27
III	$Pd(CN)_2 \cdot nH_2O$ (Aldrich as purchased)	H_2O	30 × 30[a] 50 × 50[b]	0.29[a] 0.18[b]	0.44
IV	$Pd(CN)_2 \cdot nH_2O$ (hydrothermally treated (III))	H_2O	80 × 80[a] 90 × 90[b]	0.12[a] 0.11[b]	0.19
V	$Pd(CN)_2 \cdot nNH_3$ (heated *cis*-$Pd(CN)_2(NH_3)_2$)	NH_3	20 × 20[a] 30 × 30[b]	0.40[a] 0.29[b]	0.40
VI	$Pd(CN)_2 \cdot nNH_3$ (*cis*-$Pd(CN)_2(NH_3)_2$ + AcOH)	NH_3	25 × 25[a] 40 × 40[b]	0.33[a] 0.22[b]	N/A[d]
VII	$Pt(CN)_2 \cdot nNH_3$ (heated *cis*-$Pt(CN)_2(NH_3)_2$)	NH_3	15 × 15[a] 25 × 25[b]	0.50[a] 0.33[b]	N/A
VIII	$Pt(CN)_2 \cdot nH_2O$ (precipitate from $K_2Pt(CN)_4 + K_2PtCl_4$)	H_2O	10 × 10[a] 20 × 20[b]	0.67[a] 0.40[b]	0.57
IX	$Pd_{1/2}Pt_{1/2}(CN)_2 \cdot nH_2O$ (precipitate from $K_2Pd(CN)_4 + K_2PtCl_4$)	H_2O	15 × 15[a] 30 × 30[b]	0.50[a] 0.29[b]	0.30

[a] Sheet size determined from X-ray modeling with composition derived from Table 2. [b] Sheet size determined from Scherrer eqn[7] with composition derived from Table 2. [c] Composition determined from thermogravimetric analysis. [d] Sample contained acetic acid impurity so *n* was not determined from thermogravimetric analysis.

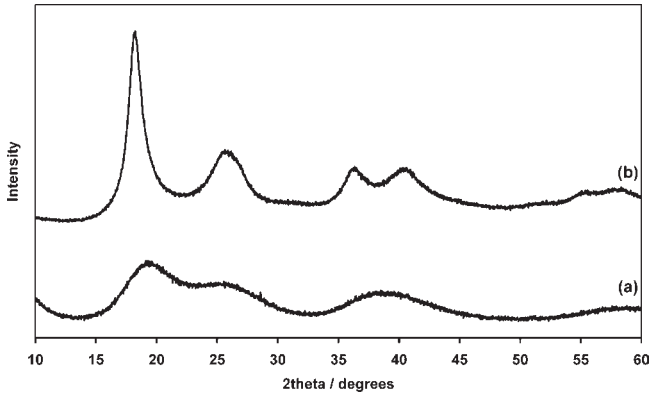

Figure 11. Experimental XRD patterns of (a) $Pt(CN)_2 \cdot 0.67H_2O$ (**VIII**) (sheet size 10 Å × 10 Å) and (b) $Pt(CN)_2 \cdot 0.29NH_3$ (**II**) (sheet size 30 Å × 30 Å).

cyanides would occur if the sheets were of infinite extent. The two types can indeed be distinguished in the IR spectra as $\upsilon(CN)_{bridging}$ modes occur at ~2220 cm^{-1} and $\upsilon(CN)_{terminal}$ modes at ~2160 cm^{-1}. The latter have stretching frequencies close to those found in the $[M(CN)_4]^{2-}$ ions[17] and in *cis*-$M(CN)_2(NH_3)_2$ (M = Pd (Figure 15),[18] Pt[19]). On decreasing the sheet size, the relative absorbance of the terminal to bridging $\upsilon(CN)$ modes increases, as predicted in Table 2. This is most clearly seen in Figure 14 for $Pd(CN)_2 \cdot 0.29H_2O$ (**I**) and $Pt(CN)_2 \cdot 0.67H_2O$ (**VIII**) which have sheet sizes of 30 Å × 30 Å and 10 Å × 10 Å, respectively. That the number of terminal water groups increases as the sheet size is reduced can also be seen from the change in relative absorbance of the $\delta(OH_2)$ to $\upsilon(CN)_{bridging}$ modes.

The Raman spectra, although rather insensitive to vibrations involving ammonia and water, are consistent with the above observations and interpretation. Both $\upsilon(CN)_{bridging}$ and $\upsilon(CN)_{terminal}$ modes can be seen (Figure 16), and changes in their relative intensities again reflect changes in the sheet sizes. The ratio of the peaks intensities of $\upsilon(CN)_{terminal}$: $\upsilon(CN)_{bridging}$ modes is however lower in the Raman than the IR spectra. In $Pd(CN)_2 \cdot 0.29H_2O$ (**I**), there are two $\upsilon(CN)_{bridging}$ frequencies observed in the Raman spectrum. These, together with the

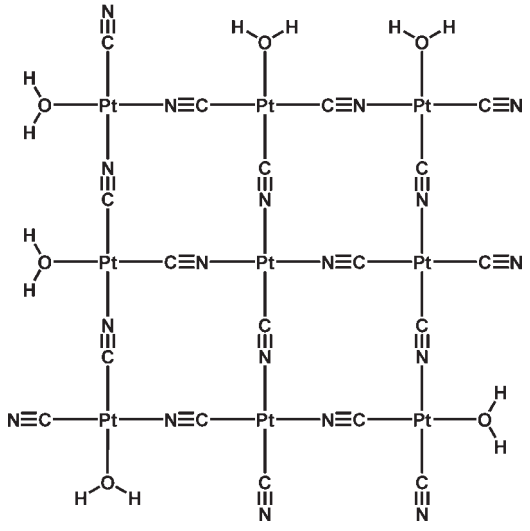

Figure 12. Nanosheet of 10 Å × 10 Å (2 × 2 Pt−CN−Pt repeat units) found in $Pt(CN)_2 \cdot 0.67H_2O$ (**VIII**) with water molecules as sheet-terminating groups.

(17) Kubas, G. J.; Jones, L. H. *Inorg. Chem.* **1974**, *13*, 2816.
(18) Soptrajanova, L.; Soptrajanova, B.; Jovanovski, G. *J. Mol. Struct.* **1986**, *142*, 63.
(19) Kharitonov, Y. Y.; Evstafeva, O. N.; Baranovskii, I. B.; Mazo, G. Y. *Russ. J. Inorg. Chem.* **1969**, *14*, 248.

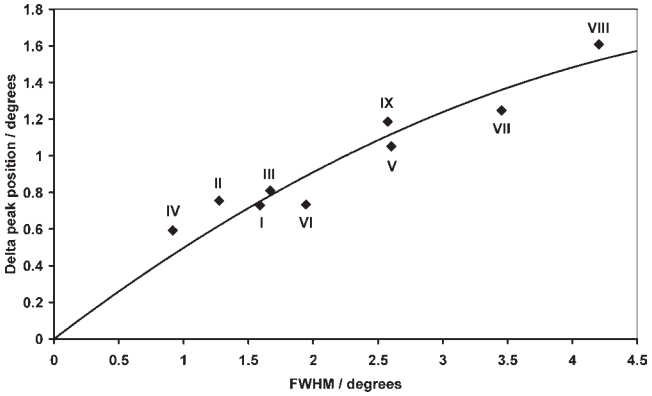

Figure 13. Measured shift in the (*10*) peaks in the powder XRD patterns for compounds (**I**)−(**IX**) (as defined in Table 4) from those calculated for the theoretical infinite $M(CN)_2$ sheets (M = Pd, Pt) as a function of the peak width (i.e., a measure of the particle size). The solid line is an aid to the eye. The sheet sizes are as follows: (**IV**): 80 Å × 80 Å; (**I**)−(**III**): 30 Å × 30 Å; (**VI**): 25 Å × 25 Å; (**V**): 20 Å × 20 Å; (**VII**) and (**IX**): 15 Å × 15 Å; (**VIII**): 10 Å × 10 Å.

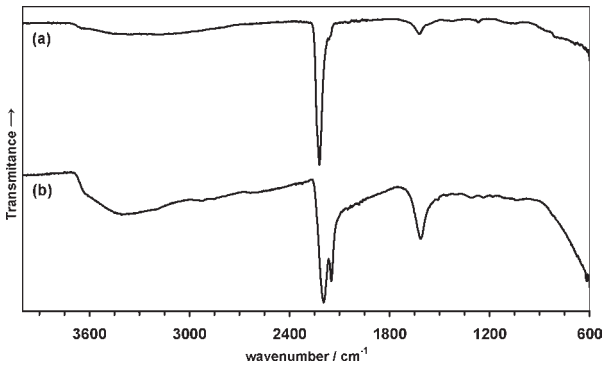

Figure 14. Infrared spectra of (a) $Pd(CN)_2 \cdot 0.29H_2O$ (**I**) and (b) $Pt(CN)_2 \cdot 0.67H_2O$ (**VIII**).

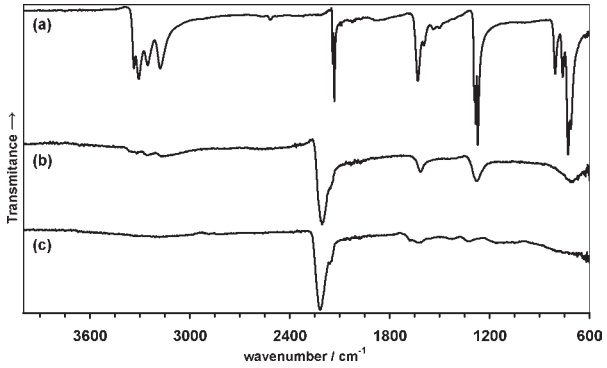

Figure 15. Infrared spectra of (a) *cis*-$Pd(CN)_2(NH_3)_2$, (b) $Pd(CN)_2 \cdot 0.40NH_3$ (**V**), and (c) $Pt(CN)_2 \cdot 0.29NH_3$(**II**).

single non-coincident $\upsilon(CN)_{bridging}$ peak in the IR spectrum, reflect the square-planar coordination around the metal centers in the interior of the sheet. In the Raman spectrum of $Pt(CN)_2 \cdot 0.67H_2O$ (**VIII**), the different $\upsilon(CN)_{bridging}$ modes are not fully resolved. We ascribe this to an increase in the widths of the peaks due to the reduced sheet size.

Electron Microscopy Studies. Electron microscopy studies proved difficult because of the beam sensitivity of the samples. Exposure to the electron beam rapidly led to decomposition and production of metallic palladium

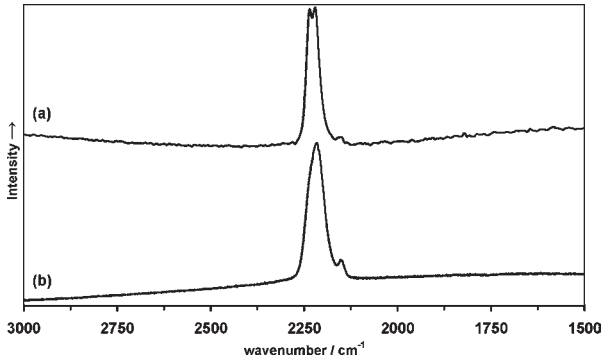

Figure 16. Raman spectra of (a) $Pd(CN)_2 \cdot 0.29H_2O$ (**I**) and (b) $Pt(CN)_2 \cdot 0.67H_2O$ (**VIII**).

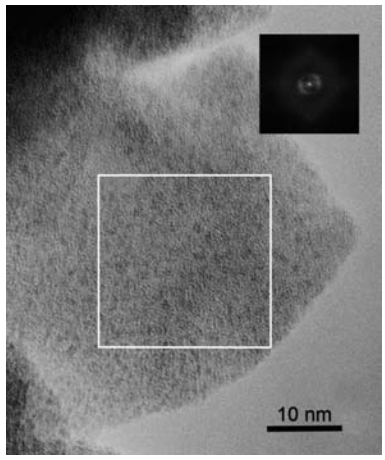

Figure 17. High resolution TEM image of an agglomeration of $Pt(CN)_2 \cdot 0.67H_2O$ (**VIII**) particles. Inset shows the diffraction pattern generated by Fourier transformation of the image in the square bounded by the white lines. The diffraction pattern ring at 0.21 $Å^{-1}$ shows a periodicity of 4.7 Å in the image.

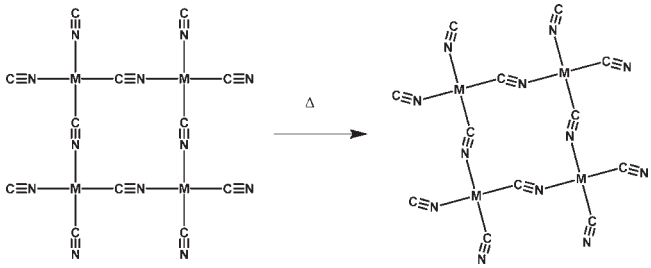

Figure 18. Distortion of the $M(CN)_2$ sheet on heating leading to a decrease in the M···M distances and 2-D negative thermal expansion (2D-NTE) within the sheet.

or platinum. Supporting Information, Figure S14 shows an image in which small palladium particles in a sample of $Pd(CN)_2.0.33NH_3$ (**VI**) identified by the fringe spacing of 2.2 Å, are seen. The size of the palladium particles, ∼20 to 30 Å, gives indirect evidence of the size of the palladium cyanide particles from which they originated (∼25 Å). Figure 17 shows an image of an agglomeration of $Pt(CN)_2 \cdot 0.67H_2O$ (**VIII**) particles, together with the corresponding diffraction pattern generated by Fourier transformation. The Fourier transform reveals a periodicity of 4.7 Å, consistent with the position of the first peak, the (*10*) reflection, observed in the XRD pattern in Figure 11a, confirming that in this particular case, the sample has not decomposed but the imaged sample

is platinum cyanide. Unfortunately, the square particles anticipated from our other studies are not seen as individual entities. However, the image and electron diffraction pattern are consistent with the information on crystallite size obtained using other methods.

Conclusions

Palladium and platinum cyanides have turned out not to be simple extended solids, as was originally envisaged, but are nanocrystalline materials consisting of small sheets of vertex sharing square-planar $M(CN)_4$ units of sheet sizes ranging from 10 Å × 10 Å to 80 Å × 80 Å. It has proved possible not only to determine the structure of the interior of the sheets, but also to show how charge neutrality can be maintained by incorporating either water or ammonia molecules in some of the terminal positions. Thus we are now in a position to represent the structures of palladium and platinum cyanides as large molecules (Figure 12). We would expect from our previous work on nickel cyanide to observe two-dimensional (2-D) negative thermal expansion (NTE) in palladium and platinum cyanides. This is indeed the case: α_a[20] has values of -8.05×10^{-6} and -5.30×10^{-6} K^{-1} for compounds (**I**) and (**II**), comparable with $\alpha_a = -6.5(1)\times10^{-6}$ K^{-1} for $Ni(CN)_2$.[2] These materials provide an opportunity to study effects such as NTE in the crossover regime between large molecules and extended solids. Figure 18 shows one of the types of motions likely to be responsible for the NTE effect seen in these materials.

It can now be seen why it has taken so long to verify that Pauling's proposed structure for palladium and platinum cyanides is essentially correct. The materials studied to date, including those examined in this work, are more complex than originally assumed. They are in fact not stoichiometric $Pd(CN)_2$ or $Pt(CN)_2$, but always contain ammonia or water molecules at the edges of nanosheets. Using the range of techniques employed in this paper however, we have been able to show how and why these molecules are bound. We have been able to vary the sizes of the nanosheets within limited bounds, and our next goal is to extend both the chemistry and size of the sheets.

Experimental Section

All samples were characterized using powder XRD, IR, and Raman spectroscopy and thermogravimetric and differential thermal analysis. Powder XRD data were collected using a Bruker D8 Advanced diffractometer ($Cu-K\alpha_1$ radiation) operating in Bragg−Brentano geometry with a Lynx-Eye detector. IR and Raman spectra were collected from undiluted powders using a Perkin-Elmer spectrum 100 FT-IR spectrometer with a Universal Attenuated Total Reflection sampling accessory and a Renishaw InVia Raman microscope (λ = 532 or 785 nm), respectively. Thermal analyses were performed under dry N_2 using a TA Q600 STD simultaneous TGA/DTA instrument at a heating rate of 1 °C min^{-1}. Small samples were decomposed to metal and cyanogen gas, typically over the temperature range 20−600 °C. Single-crystal X-ray structure determinations were carried out using a Gemini S Ultra diffractometer (graphite-monochromated Mo−Kα radiation). Densities were measured using a Quantachrome Micropycnometer at room temperature. Transmission electron microscopy studies were performed using a JEOL 2010 electron microscope, with a point resolution of 0.19 nm, operating at an accelerating voltage of 200 kV. Specimens were prepared by dispersing the samples in chloroform and depositing onto holey carbon films. As far as possible, exposure of the specimens to an intense electron beam was avoided, to minimize beam damage, but this still proved problematical with samples decomposing to form the metal.

Sample Preparation. ***Caution!*** *Cyanide materials are toxic and must be handled with care, particularly when gram quantities, which are required for neutron scattering studies, are being prepared.*

Palladium and Platinum Cyanides for Neutron Studies, $Pd(CN)_2\cdot xH_2O$ and $Pt(CN)_2\cdot yNH_3$. $Pd(CN)_2\cdot0.29H_2O$ (I). A sample purchased as $Pd(CN)_2$ from Aldrich (6 g) as an off-white powder (**III**) was dried under vacuum at 120 °C for 3 h to produce (**I**) (Figure 2). The IR spectrum (Figure 14) showed the presence of water in the material. The neutron analysis results, supported by thermal analysis, gave the composition of the dried sample (**I**) as $Pd(CN)_2\cdot0.29H_2O$ (Tables 3 and 4, Supporting Information, Figure S7). The pycnometrically measured density was 2.81 g cm^{-3}.

IR (Figure 14): υ(OH) 3165 (vvw, v broad); υ(CN) 2220(s), 2164(w); $\delta(OH_2)$ 1623(w), $\rho(OH_2)$ 1040 (vvw, broad); υ(PdC, PdN) 554(s) cm^{-1}.

Raman (Figure 16): υ(CN) 2240(s), 2224(s), 2153(vw); υ(PdC, PdN) 565(vw), 468(vw); low frequency bends: 360(vw), 322(vw), 231(vw) cm^{-1}.

$Pt(CN)_2\cdot0.29NH_3$ (II). (**II**) was prepared as a yellow powder by decomposition of $(NH_4)_2Pt(CN)_4\cdot2H_2O$ at 300 °C under vacuum for 17 h.[21] The ammonium salt was first prepared by mixing solutions of $BaPt(CN)_4\cdot2.6H_2O$ (Aldrich) (7.3875 g, 15.28 mmol) in H_2O (110 mL) and $(NH_4)_2SO_4$ (2.2363 g, 16.92 mmol) in H_2O (10 mL) at room temperature. The immediate precipitate, $BaSO_4$, was filtered off, and the remaining solution allowed to evaporate almost to dryness at room temperature over a few days to produce bright yellow crystals of $(NH_4)_2Pt(CN)_4\cdot2H_2O$ (lattice parameters at 150 K: a = 6.502(3), b = 14.508(1), c = 11.070(1) Å; spacegroup $Pna2_1$) contaminated with $(NH_4)_2SO_4$. The ammonium sulfate in the solid was removed by sublimation during the decomposition of the ammonium palatinate to form compound (**II**) (Figure 2). The IR spectrum (Figure 15) showed the presence of ammonia in the material. Analysis of the neutron data, together with thermal analysis (Supporting Information, Figure S8), gave the composition of the sample as $Pt(CN)_2\cdot0.29NH_3$. The pycnometrically measured density was 4.32 g cm^{-3}.

IR (Figure 15): υ(NH) 3200 (vw, v broad); υ(CN) 2217(s), 2158(m); $\delta_{as}(NH_3)$ 1675(w), 1625(w); $\delta_s(NH_3)$ 1322(w) cm^{-1}.

Raman: not collected, sample fluoresced.

Palladium Cyanides, $Pd(CN)_2\cdot xH_2O$ and $Pd(CN)_2\cdot pNH_3$. $Pd(CN)_2\cdot xH_2O$ (III) and (IV). The effect of hydrothermal treatment on the particle size of $Pd(CN)_2\cdot xH_2O$ was investigated. $Pd(CN)_2$ from Aldrich (0.0311 g, 0.1962 mmol) (**III**) was heated in an autoclave with H_2O (5 mL) in the presence of a small quantity of KCN (0.0056 g, 0.086 mmol), to act as a mineralizer, at 150 °C for 4 weeks. The powder XRD pattern of the product (**IV**) showed some sharpening of the peaks (Supporting Information, Figure S5), consistent with an increase in sheet size from 30 Å × 30 Å to 80 Å × 80 Å (Table 4). TGA data are shown in Supporting Information, Figures S9 and S10, respectively.

(**III**) IR: υ(CN) 2217(s), 2165(w); $\delta(OH_2)$ 1622(w); $\rho(OH_2)$ 1037(w, broad); υ(PdC, PdN) 550(s) cm^{-1}.

(**III**) Raman: υ(CN) 2238(s), 2224(s); υ(PdC, PdN) 558 (vvw), 470(vvw); low frequency bend: 362(vvw) cm^{-1}.

(**IV**) IR: υ(OH) 3350 (vw, v broad); υ(CN) 2234(s), 2220(s), 2154(w); $\delta(OH_2)$ 1623(w); $\rho(OH_2)$ 1030(vvw, broad); υ(PdC, PdN) 550(s) cm^{-1}.

***cis*-$Pd(CN)_2(NH_3)_2$** was prepared for use as a crystalline precursor to $Pd(CN)_2\cdot pNH_3$ by dissolving $Pd(CN)_2$ (Aldrich) (0.1572 g, 0.9921 mmol) in aqueous NH_3 (35%, 50 mL). After 3 days, crystals in the form of colorless needles grew in the solution. The crystals were filtered off and allowed to dry in air.

(20) Coefficient of thermal expansion for a parameter l is given by $\alpha_l = (l_T - l_0)/l_0(T - T_0)$, where l_T is the parameter l at temperature T and l_0 is the parameter l at T_0.

(21) Grünberg, A. *Izv. Inst. Izuch. Platiny* **1928**, *6*, 155.

A full structure determination confirmed that the crystals were *cis*-$Pd(CN)_2(NH_3)_2$ (lattice parameters at 150 K: a = 6.7416(3), b = 12.6824(4), c = 6.7431(3) Å; β = 110.675(5)°; spacegroup $P2_1/n$)[22] and the IR spectrum was in close agreement with that reported by Šoptrajanova et al.[18]

IR (Figure 15): υ(NH) 3344(m), 3306(m), 3252(m), 3177(m); υ(CN) 2143(m), 2133(s); $\delta_{as}(NH_3)$ 1629(s), 1592(w); $\delta_s(NH_3)$ 1288(s), 1284(s), 1271(s); $\rho(NH_3)$ 805(m), 760(m), 727(s), 710(s) cm^{-1}.

Raman: υ(CN) 2146(s), 2135(mw); $\delta_s(NH_3)$ 1284(vw), 1267(vw), 1099(vw, broad); υ(PdC, PdN) 489(vw), 469(mw), 435(vw), 414(vvw), 399(vw); low frequency bends: 378(vvw), 263(w), 150(w) cm^{-1}.

$Pd(CN)_2 \cdot pNH_3$ (V) and (VI). (**V**) and (**VI**) were prepared from *cis*-$Pd(CN)_2(NH_3)_2$ by two methods:

(a) Heating crystals of *cis*-$Pd(CN)_2(NH_3)_2$ under nitrogen in the thermogravimetric apparatus from 20 to 200 °C led to the evolution of ammonia and the formation of nanocrystalline $Pd(CN)_2.0.40NH_3$ (Table 4, Supporting Information, Figure S11) (**V**).

IR (Figure 15): υ(NH) 3326(w), 3243(w), 3144(w); υ(CN) 2205(s), 2154(m); $\delta_{as}(NH_3)$ 1609(m); $\delta_s(NH_3)$ 1270(ms); υ(PdC, PdN) 696(m) cm^{-1}.

Raman: υ(NH) 3271(w), 3190(w); υ(CN) 2217(s), 2154(w); $\delta_s(NH_3)$ 1296(w); υ(PdC, PdN) 559(w), 495(mw), 471(mw); low frequency bend: 361(w) cm^{-1}.

(b) Crystals of *cis*-$Pd(CN)_2(NH_3)_2$ (0.0415 g, 0.2155 mmol) were added to aqueous CH_3CO_2H (10 mL, 1.5 M) and left for 15 weeks.[23] A powder XRD pattern showed that the white product, which retained the morphology of the original needles, was nanocrystalline. The sheet size, as determined by the X-ray modeling (Table 4), corresponds to the composition $Pd(CN)_2.0.33NH_3$ (**VI**). The IR spectrum showed that the product contained peaks corresponding to acetic acid impurity and hence the composition was not determined by thermal analysis.

IR: υ(NH) 3050(w, v broad); υ(CN) 2213(s), 2159(m); $\delta_{as}(NH_3)$ 1618(w); $\delta_s(NH_3)$ 1272(w) cm^{-1}. (Note: additional peaks due to acetic acid have been omitted).

Raman: υ(CN) 2222(s), 2158(w); υ(PdC, PdN) 565(w), 495(vw), 471(w); low frequency bends: 359(vw), 238(vw) cm^{-1}.

Platinum Cyanides, $Pt(CN)_2 \cdot qH_2O$ and $Pt(CN)_2 \cdot yNH_3$. $Pt(CN)_2 \cdot 0.50NH_3$ (VII). (**VII**) was prepared as an orange-brown solid by heating the solid produced by the evaporation of a solution of $Pt(CN)_2$ (Aldrich, 0.2463 g, 0.9967 mmol) in aqueous NH_3 (35%, 50 mL) under N_2 to 240 °C. The composition given is that corresponding to the sheet size of 15 Å × 15 Å, as determined by the X-ray modeling (Table 4).

$Pt(CN)_2 \cdot 0.67H_2O$ (VIII). (**VIII**) was prepared by adding a solution of $K_2Pt(CN)_4$ (0.1887 g, 0.5001 mmol, in 5 mL water) to a solution of K_2PtCl_4 (0.2078 g, 0.5006 mmol, in 5 mL water). A yellow-brown gel formed over a period of two to three weeks. This was repeatedly washed with water and allowed to dry in air. The reflections in the powder XRD pattern were very broad (Figure 11), consistent with the very small sheet size, 10 Å × 10 Å, of this sample (Table 4). TGA data are shown in Supporting Information, Figure S12.

IR (Figure 14): υ(OH) 3440(w, v broad); υ(CN) 2201(s), 2152(s); $\delta(OH_2)$ 1611(w) cm^{-1}.

Raman (Figure 16): υ(CN) 2216(vs), 2151(w); υ(PtC, PtN) 616(w, broad), 504(w), 477(w); low frequency bend: 357(w) cm^{-1}.

Mixed Palladium−Platinum Cyanide, $Pd_{1/2}Pt_{1/2}(CN)_2 \cdot xH_2O$. $Pd_{1/2}Pt_{1/2}(CN)_2 \cdot 0.50H_2O$ (IX). (**IX**), a nanocrystalline mixed palladium−platinum cyanide, was prepared by adding a solution of $K_2Pd(CN)_4$ (0.1447 g, 0.5012 mmol, in 5 mL water) to a solution of K_2PtCl_4 (0.2078 g, 0.5006 mmol, in 5 mL water). A cream powder formed over a period of 6 to 8 weeks. This was filtered, repeatedly washed with water, and allowed to dry in air. The powder XRD pattern is given in Supporting Information, Figure S.6. Thermogravimetric analysis gave the composition as $Pd_{1/2}Pt_{1/2}(CN)_2 \cdot 0.39H_2O$ (Table 4, Supporting Information, Figure S13), in reasonable agreement with the composition determined from the X-ray modeling. The powder XRD pattern of the final product after heating could be indexed on the basis of a cubic unit cell with lattice parameter a = 3.9036(2) Å, in excellent agreement with the value of 3.903 Å found for the alloy $Pd_{1/2}Pt_{1/2}$.[24]

IR: υ(OH) 3400(w, very broad); υ(CN) 2202(s), 2150(m); $\delta(OH_2)$ 1614(m); $\rho(OH_2)$ 1089(w, broad) cm^{-1}.

Raman: υ(CN) 2219(vs), 2151(w); υ(Pd/PtC, Pd/PtN) 598(w, broad), 472(w); low frequency bend: 348(w) cm^{-1}.

Neutron Diffraction Experiments. Time-of-flight powder neutron diffraction intensities were measured at 10 and 300 K for $Pd(CN)_2 \cdot 0.29H_2O$ (**I**) and $Pt(CN)_2 \cdot 0.29NH_3$ (**II**) on the GEM diffractometer[25] at the ISIS Facility, Rutherford Appleton Laboratory, Chilton, Didcot, U.K. Samples of $Pd(CN)_2 \cdot 0.29H_2O$ (**I**) (5.0051 g) and $Pt(CN)_2 \cdot 0.29NH_3$ (**II**) (3.6740 g) were loaded into cylindrical 11 mm diameter drawn vanadium cans, under argon, in a glovebox.

The packing density of each sample, as used in the data correction routines, was determined from the sample depth and can diameter. Background runs were collected on the empty can and empty spectrometer and absolute normalization data were collected for a standard vanadium rod.

Analysis of Neutron Diffraction Data. The total neutron diffraction data were obtained from four detector banks (banks 2, 3, 4, 5 at average scattering angles of 17.3, 34.3, 61.7, and 91.8°). Correction for multiple scattering, attenuation, and inelasticity, and normalization to absolute scattering units was performed using the ATLAS[26] and GUDRUN[27] suites of programs (see Supporting Information). The presence of hydrogen in both palladium and platinum samples was evident from the variation of the total scattering as a function of scattering angle. The hydrogen content of the palladium sample was estimated to be ~2/3 that of the platinum sample per $M(CN)_2$ formula unit. The contribution from the incoherent scattering due to hydrogen was then removed by subtracting a linear term to ensure that the total scattering oscillated about the calculated self-scattering. The corrected and normalized data from the four detector banks were merged in each case to yield an interference function, $Qi(Q)$ (Supporting Information, Figure S1), which covered the Q range 0.8−44 $Å^{-1}$, and this was then extrapolated to Q = 0 $Å^{-1}$.

Acknowledgment. The authors thank the EPSRC for Research Studentships for E.J.B. and E.M. and for a single-crystal X-ray diffractometer in Reading (Grant EP/533526/1). The University of Reading is acknowledged for provision of the Chemical Analysis Facility (CAF) and the Centre for Analysis and Microscopy (CFAM) and the Nuffield Foundation for an undergraduate bursary for Junjuda Unruangsri, who performed some of the preliminary syntheses.

Supporting Information Available: Details of total neutron scattering analysis for (**I**) and (**II**), TGA data for (**I**) and (**II**), powder X-ray data for(**IV**) and (**IX**) with modeling of palladium-cyanide sheets. This material is available free of charge via the Internet at http://pubs.acs.org.

(22) Penavić, M.; Šoptrajanova, L.; Jovanovski, G.; Šoptrajanov, B. *Acta Crystallogr.* **1986**, *C42*, 1283.
(23) Gillard, R. D. *J. Inorg. Nucl. Chem.* **1965**, *21*, 1321.
(24) Darby, J. B.; Myles, K. M. *Metall. Trans.* **1972**, *3*, 653.
(25) Hannon, A. C. *Nucl. Instrum. Meth.* **2005**, *A551*, 88.
(26) Hannon, A. C.; Howells, W. S.; Soper, A. K. In *Institute of Physics Conference Series*; Johnson, M. W., Ed.; IOP Publishing Ltd.: Bristol, 1990; Vol. *107*, pp 193−211.
(27) McLain, S. E.; Bowron, D. T.; Hannon, A. C.; Soper, A. K. *GUDRUN: a computer program developed for analysis of neutron diffraction data*; see http://www.isis.rl.ac.uk/disordered/Manuals/gudrun/Gudrun_manual_2006.pdf.